FULL PAPER

Magnetic Resonance in Medicine 00:00–00 (2016)

Detection of Smoke-Induced Pulmonary Lesions by Hyperpolarized ^{129}Xe Diffusion Kurtosis Imaging in Rat Models

Weiwei Ruan,[1,2] Jianping Zhong,[1] Yu Guan,[3] Yi Xia,[3] Xiuchao Zhao,[1] Yeqing Han,[1] Xianping Sun,[1,2] Shiyuan Liu,[3] Chaohui Ye,[1,2] and Xin Zhou[1,2]*

Purpose: To demonstrate that hyperpolarized (HP) xenon diffusion kurtosis imaging (DKI) is able to detect smoke-induced pulmonary lesions in rat models.

Methods: Multi-b DKI with hyperpolarized xenon was used for the first time in five smoke-exposed rats and five healthy rats. Additionally, DKI with b values of up to 80 s/cm^2 were used in two healthy rats to probe the critical b value (a limit beyond which the DKI cannot describe the non-Gaussian diffusion).

Results: The mean apparent diffusion coefficient (D_{app}) and diffusion kurtosis (K_{app}) extracted by the DKI model revealed significant changes in the smoke-exposed rats compared with those in the control group ($P = 0.027$ and 0.039, respectively), exhibiting strong correlations with mean linear intercept (L_m) from the histology. Although the maximum b value was increased to 80 s/cm^2, the DKI could still describe the non-Gaussian diffusion ($R^2 > 0.97$).

Conclusion: DKI with hyperpolarized xenon exhibited sensitivity in the detection of pulmonary lesions induced by smoke, including moderate emphysema and small airway diseases. The critical b value was rarely exceeded in DKI of the lungs due to the limited gradient strength of the MRI scanner used in our study. **Magn Reson Med 000:000–000, 2016.** © **2016 International Society for Magnetic Resonance in Medicine.**

Key words: hyperpolarized xenon; DKI; smoke; D_{app}; K_{app}; pulmonary lesions

INTRODUCTION

Exposure to cigarette smoke is an established cause of chronic obstructive pulmonary disease (COPD) (1), lung cancer (2), and cardiovascular disease (3) in cigarette smokers. However, the causal relationship between exposure to smoke and the development of COPD remains unclear (4).

COPD, which is characterized by a persistent airflow limitation caused by a mixture of small airway diseases and parenchymal destruction, is currently the fourth-leading cause of death among adults worldwide (5). The most common diagnostic tools for COPD are pulmonary function tests. However, pulmonary function tests can only assess global pulmonary function and cannot provide the localized regions of abnormality. Moreover, they are insensitive for detecting small airway diseases (6,7), which could miss the early detection of lung diseases. High-resolution computed tomography (CT) has also been used to detect diseased areas of the lungs with COPD due to abnormal x-ray attenuation, but the precise separation of fully expanded normal lung from mild emphysema using CT remains a subject of debate (8). Importantly, the use of CT in longitudinal studies has been limited because of exposure to ionizing radiation.

Hyperpolarized (HP) gas (^{3}He or ^{129}Xe) MRI is an emerging method to detect pulmonary disease in vivo without ionizing radiation (9–11). With the technology of laser polarization, the noble gas MR signal can be amplified 10,000 to 100,000 times more than the thermally polarized gas MR signal (11,12). When inhaling the polarized noble gas into the lung, MR images of the lung airspace can be obtained. Initial successful application of the method to detect pulmonary disease has been demonstrated by imaging in the absence or presence of gas (density imaging), thus showing ventilation defects in the lung (13–15). However, this technique was insensitive to the microstructural changes in the lung due to the limited spatial resolution, especially using ^{129}Xe, which has a smaller gyromagnetic ratio and is more difficult to be polarized than ^{3}He. Hyperpolarized gas diffusion MRI of the lungs has shown remarkable sensitivity to pulmonary microstructural changes (16,17). Initially, the apparent diffusion coefficients (ADCs) of HP gas in the lung were measured to reflect the changes in the pulmonary microstructure at the alveolar level through the traditional Gaussian diffusion equation (16–19)

$$\mathrm{ADC} = (-1/b)\ln(S/S_0), \quad [1]$$

where b is the factor of diffusion sense, S is the image with diffusion gradient, and S_0 is the image without diffusion gradient. However, the microstructure of the lung is quite complex. In humans, there are 14 generations of

[1]Key Laboratory of Magnetic Resonance in Biological Systems, State Key Laboratory of Magnetic Resonance and Atomic and Molecular Physics, National Center for Magnetic Resonance in Wuhan, Wuhan Institute of Physics and Mathematics, Chinese Academy of Sciences, Wuhan, P. R. China.

[2]University of Chinese Academy of Sciences, Beijing, P. R. China.

[3]Department of Radiology, Changzheng Hospital of the Second Military Medical University, Shanghai, China.

Grant sponsor: National Natural Science Foundation of China; Grant numbers: 81227902 and 81625011; Grant sponsor: National Program for Special Support of Eminent Professionals (National Program for Support of Top-notch Young Professionals).

*Correspondence to: Xin Zhou, Ph.D. Professor, Wuhan Institute of Physics and Mathematics, Chinese Academy of Sciences, 30 West Xiaohongshan, Wuhan, China. E-mail: xinzhou@wipm.ac.cn

Received 30 May 2016; revised 3 November 2016; accepted 9 November 2016

DOI 10.1002/mrm.26566

Published online 00 Month 2016 in Wiley Online Library (wileyonlinelibrary.com).

airways prior to the terminal bronchioles, and another nine inside the acini (20). Meanwhile, diffusion of HP gas is very fast. In the homogeneous and unrestricted spaces, the diffusion coefficients are 0.88 cm^2/s for highly diluted helium gas and 0.14 cm^2/s for diluted xenon gas (21), which will diffuse over average distances of approximately 0.9 mm (helium) and 0.4 mm (xenon), over the 5 ms diffusion time. In comparison, the diameters of the respiratory bronchioles and alveoli are a few hundred micrometers in humans (20,21) and tens of micrometers in rodents (22,23). The diffusion of HP gas in the lung has exhibited restricted and anisotropic behavior at the alveolar level, resulting in a substantial deviation from a Gaussian phase distribution. This deviation is manifested through nonexponential signal decay with increasing b values—that is, the diffusion of HP gas in the lung has been shown to be non-Gaussian (7,20,24).

Diffusion kurtosis imaging (DKI) has been established as a powerful proton MRI technique to describe non-Gaussian diffusion, which uses kurtosis, a general dimensionless metric, to quantify the non-Gaussian characteristics of spin-bearing particle diffusion processes (25). Non-Gaussian behavior is usually associated with complex tissues and exists where structure barriers are present, such as cell membranes, organelles, or pulmonary alveoli. In this way, DKI provides a method of detecting these complex tissues or structures. The non-Gaussian diffusion was first discovered in nonimaging NMR investigations by Tanner and Stejskal (26) in 1968. Jensen et al. (27) first suggested the definition of diffusional kurtosis and extracted the kurtosis from the characteristic signal attenuation with multi-b value diffusion-weighted MRI in 2005. The original applications of DKI in human tissue focused mainly on brain imaging (28,29). In recent years, DKI technology has been studied widely and has been highly developed, extending from studies of the brain to other tissues, such as the bladder (30), kidney (31), and prostate (32). Trampel et al. (7) also used DKI measurement of hyperpolarized ^{3}He in healthy human subjects and one patient with symptoms suggestive of small airway disease. The results demonstrated that DKI could well describe the non-Gaussian distribution of HP ^{3}He diffusion in the human lung. The ADC in the patient was similar to that in the normal controls, but the diffusion kurtosis was markedly reduced. This finding suggested that HP ^{3}He DKI might be useful and more sensitive to changes in larger bronchioles and bronchi than traditional ADC measurement (7). However, the limited supply and extremely low natural abundance (~0.0137%) of ^{3}He have prevented it from being applied extensively. In contrast, the supply of ^{129}Xe is nearly unconstrained on the earth, and it has a much higher natural isotopic abundance of ~26.4% (10). Therefore, xenon is uniquely suitable for potential clinical applications in the future. To our knowledge, lung study with HP ^{129}Xe DKI has so far not been reported. In addition, Jacob et al. (24) reported previously that there existed a critical b value or an approximate limit beyond which the kurtosis approach no longer described the non-Gaussian nature of HP ^{3}He diffusion in the lung, but in vivo experiments were lacking.

In this study, eight b values (4, 8, 12, 16, 20, 24, 28, and 32 s/cm^2) for DKI were used to describe the non-Gaussian HP xenon diffusion in the lungs of five rats exposed to cigarette smoke and five healthy rats. The diffusion coefficient and the diffusion kurtosis in the lung parenchyma were all extracted to detect the pulmonary characteristics of rats exposed to cigarette smoke. The relationships between the parameters extracted from DKI and the pulmonary microstructure were analyzed, whereas the histological morphology was obtained to help analyze the DKI results. In addition, a much larger b value of up to 80 s/cm^2 HP xenon DKI was used in another two healthy rats to study the critical b value in the lung parenchyma.

METHODS

^{129}Xe Polarization and Delivery

With spin-exchange optical pumping processing, enriched xenon gas (86% ^{129}Xe) was polarized to ~10% with a home-built polarizer. The gas mixture consisted of 1% xenon, 10% N_2, and the balance of ^{4}He. First, the HP gas was polarized, and then cryogenically concentrated and stored as a solid using liquid nitrogen (33–36). Before being delivered into the lungs of the rats, the solid xenon was warmed into a gas phase and expanded into a Tedlar bag, which was rapidly connected to a home-built ventilator. In this experiment, almost 200 mL of HP xenon gas could be obtained in 40 minutes at a flow rate of 0.5 L/m.

Animal Preparation

All of the animals handling procedures were approved by the institutional animal studies committee. Twelve male Wistar rats (280 ± 30 g) were used in the study. The rats were randomly divided into the following two groups: the experimental group and the healthy group.

The experimental group included five rats in which a lung injury model was induced by cigarette smoke for 6 months according to the method described by Bai et al (37). In brief, the rats received the smoke in a cigarette smoke exposure device (PAB-S200, BLLC, Beijing, China) twice every day. For each exposure, 10 cigarettes were used to produce smoke for 1 hour, and the interval between smoke exposures was 4 hours. Single cigarette contained 12 mg of tar and 0.8 mg of nicotine. The other seven rats in the healthy group received nothing except daily food and water. Five rats were used as controls for the experimental group, and the other two rats were used in the second part of the experiment to study the critical b value for HP xenon DKI. Before MRI examination, each rat was anesthetized with 5.0% isoflurane (Keyuan Pharmaceutical, Shandong, China) and was intubated with a 14-guage endotracheal tube, which was tied to the trachea. After intubation, the rat was ventilated using a custom-built ventilator. During the experiment, the rat was alternatively ventilated with oxygen and HP xenon as shown in Figure 1. The polarization of HP xenon in a Tedlar bag always decreases due to longitudinal relaxation ($T_1 \sim 25$ min), therefore, the MRI acquisition must be accomplished as soon as possible to minimize signal loss. The total experimental time for a DKI acquisition (i.e., ventilating the rat with pure oxygen and HP xenon) was approximately 80 s. To increase the pulmonary oxygen reservoir for the rats' safety (38), the pure oxygen was used for a short time. For the oxygen, the breathing rate was 50 breaths/min with an inspiratory time of 400 ms and an

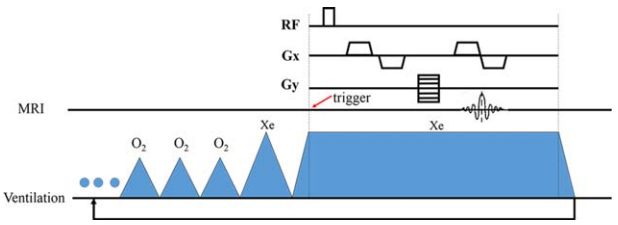

FIG. 1. Schematic diagram showing the experimental process, including ventilation and MRI sequence. Note the time to trigger the MRI acquisition when the rats were mechanically ventilated with xenon breath-hold (red arrow).

expiratory time of 800 ms. The peak inspiratory pressure was approximately 10 cm H_2O, with inspiratory capacity of approximately 2.2 mL per breath. After 5 min, the concentration of isoflurane was decreased to 3% for maintenance. For the HP xenon, the breath rate was almost 14 per minute, with an inspiratory time of 500 ms, a breath-hold time of 3000 ms, and an expiratory time of 1000 ms. The peak inspiratory pressure was 12 cm H_2O to avoid the low peak inspiratory pressure regime (<10 cm H_2O) where the diffusion was strongly dependent on lung compliance (39). The inspiratory capacity was approximately 2.5 mL per breath. The MRI acquisitions were triggered to be finished during the breath-holding of xenon as shown in Figure 1. After the acquisitions, the rats were ventilated with oxygen again.

MRI

All 2D images were acquired using a 7 T animal MRI scanner (Bruker Bio Spec 70/20 USR) equipped with a high-performance gradient coil (G = 444.75 mT/m, ramp time = 0.123 ms). A custom-built double-tuned birdcage radio frequency coil with a diameter of 5.5 cm was used in the experiment, which was operated at 298.69 MHz (^{1}H) and 83.07 MHz (^{129}Xe).

The MRI protocol was based on gradient-echo sequence, including an adjustable bipolar diffusion gradient in the frequency-encoding direction (21). The b values were given by (21,40)

$$b = \gamma^2 G^2 \left[\delta^2 \Delta - \frac{\delta}{3} + \tau \left(\delta^2 - 2\Delta\delta + \Delta t - \frac{7}{6}\delta\tau + \frac{8}{15}\tau^2 \right) \right], \quad [2]$$

where γ is the gyromagnetic ratio of ^{129}Xe, G is the strength of the diffusion gradient, τ is the ramp time of the gradient, δ is the gradient pulse width, and Δ is the diffusion time. In our experiment, $\delta = 0.8$ ms, $\Delta = 1.2$ ms, and $\tau = 0.123$ ms. For $\Delta = 1.2$ ms, the characteristic diffusion length was 120 μm, which is larger than the average alveolar length (70 μm) of healthy rats (40). The 1-ms block excitation radiofrequency (RF) pulse without slice-selection was used, and the excitation bandwidth was 1280 Hz, which ensured a minimal excitation bandwidth to cover the signals of ^{129}Xe dissolved in lung tissue and blood. The first part of the experiment used eight b values (4, 8, 12, 16, 20, 24, 28, and 32 s/cm^2) for DKI to detect the pulmonary characteristics of cigarette smoke–exposed rats. The corresponding imaging parameters were as follows: field of view = 5 × 5 cm; matrix size = 96 × 96; echo time = 3.842 ms; pulse repetition time = 9.904 ms; bandwidth = 50 kHz; and a flip angle of 9.5°. The second part, the experiment used DKI with 14 b values (4, 8, 12, 16, 20, 24, 28, 32, 40, 48, 56, 64, 72, and 80 s/cm^2) to study the critical b values in two healthy rats. Due to the limitations of the maximum gradient strength, the diffusion time Δ increased to 2.5 ms to achieve the maximum b value of 80 s/cm^2, whereas to ensure the images' signal-to-noise ratio (SNR), the matrix was decreased to 48 × 48. The echo time was 4.854 ms, and the pulse repetition time was 10.234 ms. The other parameters were kept the same with those in the first part of the experiment.

In the multi-b HP xenon diffusion experiments, except for the diffusion gradient strength, many other factors, such as T_1 relaxation, dissolution of gas into tissue and blood of lungs (41), and RF pulse, would affect the difference in signal between different b values (19). Most notably, no observable recovery of longitudinal magnetization occurred after RF pulses. To reduce these effects, three interleaved 2D gradient-echo samplings without and with diffusion weighting were acquired for a given line of k-spaces (42,43). Accordingly, for each b value, three images were obtained (i.e., two images without diffusion gradient and one image with diffusion gradient).

Image Processing and Analysis

Image processing and analysis were completed with MATLAB software (MathWorks, Natick, Massachusetts, USA). To ensure data reliability and accuracy, the original k-space data was used in the subsequent analysis.

All of the images were generated from MRI k-space using 2D discrete Fourier transform. To reduce the noise and improve the SNR of the images, all of the images were first processed with Gaussian filtering. The two images without diffusion gradients were averaged as a reference image. Then the reference image was used to generate a lung binary mask without background noise by Otsu segmentation (44), which is a common algorithm for image segmentation. The Otsu was also deemed the maximum variance between clusters based on the gray level. After that, the resulting binary mask was applied to the source images with diffusion gradients. According to the DKI relationship between the signal S and b values (7,27),

$$S = S_0^* \exp\left(-bD_{app} + \frac{1}{6} b^2 D_{app}^2 K_{app} \right), \quad [3]$$

where S_0 is the signal in the absence of the diffusion gradient, D_{app} is an estimate for the diffusion coefficient, and K_{app} is an estimate for the diffusion kurtosis. The D_{app} and K_{app} could be extracted by fitting the S/S_0 with different b values using a nonlinear least squares algorithm on a pixel-by-pixel basis for all of the rats.

In this way, the D_{app} maps and K_{app} maps were acquired for all of the rats. The seed-growing algorithm was used to segment the main tracheas and the parenchyma of the D_{app} maps because the D_{app} in the main tracheas were much larger than those in the parenchyma. Furthermore, the obtained masks were also used to segment K_{app} maps. Finally, the mean D_{app} and K_{app} values from the parenchyma were computed.

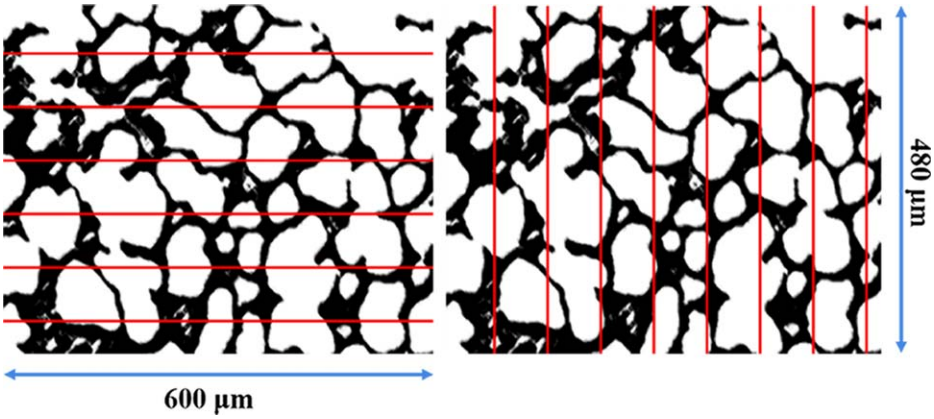

FIG. 2. Representative binary images overlapped by the horizontal and vertical grid lines, which were used to count the L_m with Image-Pro Plus software.

Quantitative Histology

After the MRI experiments, the rats were exsanguinated quickly by cuts in two sides of the femoral artery. To prevent the lung collapse when opening the thorax, the main tracheal was ligated (45). The simple tracheal ligation fixation method has been demonstrated to provide optimal lung fixation revealing the natural physiological state without apparent artifacts (45). The lungs were then extracted surgically. The extracted lungs were rinsed immediately three times with normal saline and then were preserved in a 10% paraformaldehyde solution (Sinopharm, Shanghai, China) for at least 24 h to be fixed. Finally, the extracted lungs were paraffin-embedded and sliced into hematoxylin and eosin–stained histological sections. Each lung yielded six histological sections from different regions, and each section was 10 μm thick.

The stained histological sections were coded and examined with a microscope (Nikon Eclipse Ts 100, Nikon, Tokyo, Japan), and one image per section was acquired from areas that did not contain large airways. Imaging-Pro Plus (Media Cybernetics, Rockville, Maryland, USA) software was used to calculate the mean linear intercept (L_m) with the traditional method (40,46). Because the different images were acquired on different section directions, the vertical L_m was also calculated to reduce random error. The final L_m was the mean value of the horizontal and vertical L_m, as shown in Figure 2.

Statistical Analysis

Statistical analyses were performed by using SPSS software (IBM, Armonk, New York, USA). F-variance test were used to demonstrate whether the variances of the corresponding parameters between the experimental group and the control group were homogeneity, and F values > 0.05 were considered statistically homogeneous. Afterward, an unpaired two-tailed t test was used to compare the cigarette smoke–exposed group and the control group, and the corresponding P values were calculated. P values < 0.05 were considered statistically significant. Moreover, the Pearson's correlation coefficients between the parameters extracted by DKI and the histological morphometric parameter were calculated, which were used to evaluate the relationships between the diffusion measurement and the lung microstructure.

RESULTS

Figure 3 shows three representative images (96×96) generated from the MRI k-space using two-dimensional discrete Fourier transform in one breath-hold. Figure 3a and 3c are the images without the diffusion gradients. Figure 3b is the image with $b = 32$ s/cm^2, which required nearly 80% of the maximum strength of the gradient. Due to the diffusion of the xenon atoms in the lungs, the b image is much darker than the a and c images. The SNR in the b image is still 103, which was calculated by the equation $SNR = Ms/\sigma$, where Ms is the mean value of the image signal and σ is the standard deviation of the background noise distribution (47).

Figure 4 shows the DKI model and monoexponential model fitting curves from a representative healthy rat and a smoke-exposed rat. Due to the non-Gaussian nature of xenon diffusion in the lungs, the points obviously deviated from the monoexponential curve. The $R^2 > 0.9$ in the DKI fitting demonstrated that the DKI model could describe the non-Gaussian diffusion of xenon in the pulmonary parenchyma very well.

Table 1 lists the L_m from histology and the overall mean D_{app} values and K_{app} values from pulmonary parenchyma of the five smoke-exposed rats and five healthy rats. The D_{app} and K_{app} from the parenchyma both showed significant changes in the smoke-exposed rats compared with those in the control rats ($P = 0.027$ and $P = 0.039$ for D_{app} and K_{app}, respectively), reflecting the changes in the pulmonary microstructure due to smoke for 6 months in the smoke-exposed rats. The L_m from the histology also showed a significant difference ($P = 0.013$), which demonstrated mild emphysema in the smoke-exposed rats. Two representative images of histological sections from a healthy rat and a smoke-exposed rat are shown in Figure 5, which reflect the moderate enlargement of the alveolar airspace in the smoke-exposed rat. Furthermore, the L_m from histology showed a strong correlation with the D_{app} ($r = 0.81$) and K_{app} ($r = -0.79$), indicating that the significant change of D_{app} and K_{app} were related to the emphysema in the smoke-exposed rats.

Figure 6 shows the representative maps of D_{app} (Fig. 6a, 6b) and K_{app} (Fig. 6c, 6d) from a smoke-exposed rat (Fig. 6b, 6d) and a healthy rat (Fig. 6a, 6c). The corresponding histograms were also shown under the maps. The D_{app} map and the K_{app} map in the smoke-exposed rat showed obvious differences

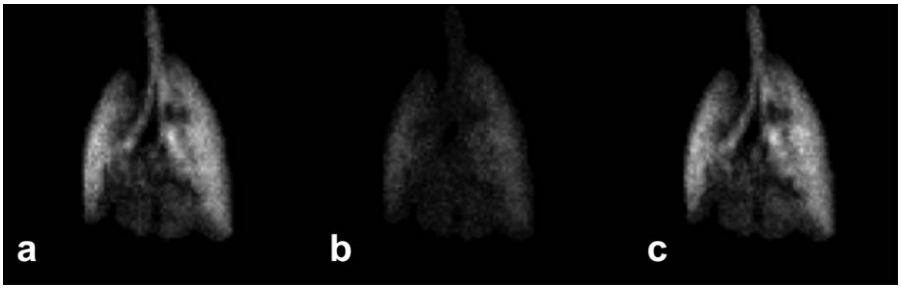

FIG. 3. Three interleaved 2D gradient echo images in one breath-hold. (**a**) First image with $b = 0$ s/cm^2. (**b**) Second image with $b = 32$ s/cm^2; the strength of the diffusion gradient almost reached 80% of the maximum gradient strength. The SNR in the image is 103. (**c**) Third image with $b = 0$ s/cm^2.

compared with that in the healthy rat. Furthermore, the D_{app} histogram in the smoke-exposed rat exhibited a much broader distribution in comparison with that in the healthy rat.

Figure 7 shows the linear correlation fittings between the D_{app} and the L_m from histology (Fig. 7a) and between the K_{app} and the L_m from histology (Fig. 7b). Note that all of the dots are between the two dashed lines, which represent 95% confidence intervals for the fit. The correlation coefficients are given in Table 1. The results demonstrated that the D_{app} and K_{app} from xenon diffusion in the lungs were highly related to pulmonary morphology.

Figure 8 displays the fitting curve of normalized signal intensities versus b values in the second part of the experiment, which studied the critical b value in the lung parenchyma. Although the maximum b value increased to 80 s/cm^2 and the maximum diffusion gradient strength increased to nearly 375 mT/m, the DKI model also could describe the non-Gaussian diffusion of xenon in the pulmonary parenchyma very well ($R^2 > 0.97$).

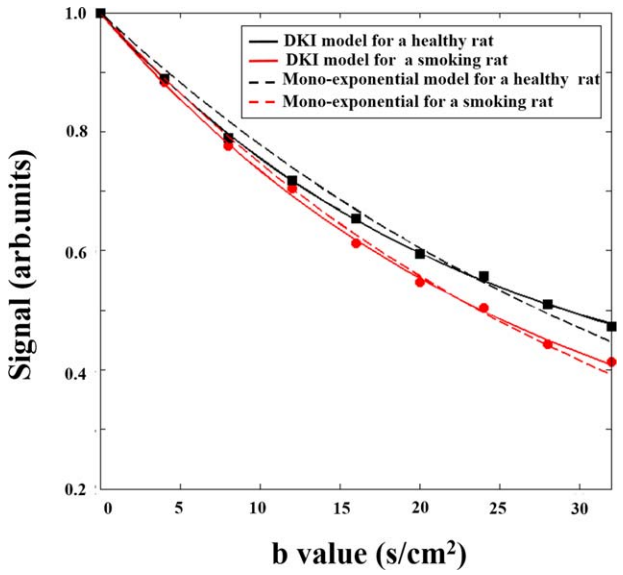

FIG. 4. Using the mean values of the whole pulmonary parenchyma, signal intensity versus b values were plotted, with the solid lines fit to a DKI model for a healthy rat (black line, $R^2 = 0.9723$) and a smoke-exposed rat (red line, $R^2 = 0.9669$). The dotted lines fit to a monoexponential model for the healthy rat (black line) and the smoke-exposed rat (red line). Note the deviation from the monoexponential curves.

DISCUSSION

Pulmonary Lesions Detection with DKI

In this study, the DKI model was used for the first time in HP xenon diffusion pulmonary MRI, and it was demonstrated to be very suitable for the description of the non-Gaussian diffusion of HP xenon, which was manifested through nonexponential signal decay with the increasing b values in the lungs of rats. Furthermore, the D_{app} and K_{app} values in the smoke-exposed rats both showed significant changes compared with those in the healthy rats, which indicated that the DKI model with HP xenon diffusion pulmonary MRI was sensitive to detect the pulmonary parenchymal changes induced by cigarette smoke. In the second part of the experiment, although the maximum b value increased to 80 s/cm^2 and the maximum gradient strength was nearly 375 mT/m, the DKI model was still very good for fitting the nonexponential signal decay in

Table 1
Mean D_{app} and K_{app} Values in the Parenchyma and L_m Values with Corresponding Statistical Data

	D_{app} (cm^2/s)	K_{app}	L_m (μm)[a]
Smoke-exposed rats	0.0355	1.0340	45.68
	0.0335	1.1260	41.27
	0.0348	1.0819	45.85
	0.0330	1.1327	38.22
	0.0313	1.1312	43.70
Mean	0.0336 ± 0.0016	1.1011 ± 0.043	42.94 ± 3.22
Control rats	0.0326	1.1685	36.80
	0.0271	1.2503	31.37
	0.0303	1.2383	38.71
	0.0313	1.1112	37.19
	0.0310	1.1431	38.96
Mean	0.0304 ± 0.0021	1.1823 ± 0.0603	36.61 ± 3.07
[b]F value	0.066	1.239	0.175
[c]*P* value	0.027	0.039	0.013
[d]Pearson's correlation coefficient	0.81	−0.79	1

[a]From histological analysis.
[b]*F* values were acquired using an *F*-variance test to demonstrate whether the variances of the corresponding parameters were homogeneous between the smoke-exposed rats and the healthy rats.
[c]*P* values were acquired using an unpaired two-tailed *t* test to demonstrate whether a significant difference existed in the corresponding parameters between the smoke-exposed rats and the healthy rats.
[d]Pearson's correlation coefficients were calculated to test the correlations of the corresponding parameters obtained by HP xenon DKI in the lungs with the L_m from histology.

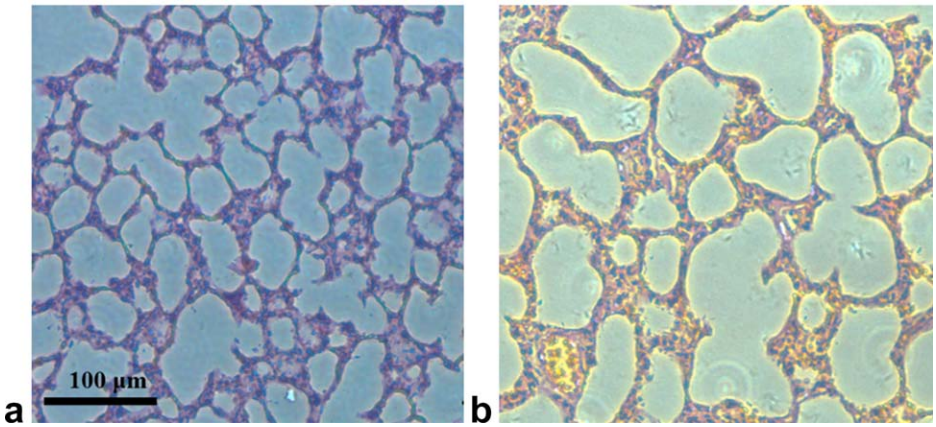

FIG. 5. Representative images of histological sections from a healthy rat (**a**) and a smoke-exposed rat (**b**). The magnification was × 200. Note the enlarged alveolar airspace in the smoke-exposed rat due to mild emphysema induced by 6 months of smoke exposure.

the other two rats ($R^2 > 0.97$). This finding indicated that limit of the critical b value for HP xenon DKI in the lungs could be ignored due to the limitation of maximum gradient strength.

Relation Between DKI and Microstructure

The traditional proton DKI can be useful to characterize tissue microstructure and its topological rearrangement and complexity (48). However, the microstructure of lung is very complex. In the branches model of lung airways, the airway tree begins at the trachea and leads through bronchi and bronchioles to the terminal bronchiole that feeds each acinus, the major gas exchange unit in the lung (20). All these structure's lesions will lead to the change of pulmonary complexity, which will increase or decrease the K_{app} values. In this study, the K_{app} showed a strong correlation with the L_m from histology, which is the clinical reference standard to evaluate the alveoli or alveolar sac. This finding indicated that the kurtosis was highly related to the status of the alveoli or alveolar sac. The enlargement of the alveolar airspace would significantly reduce the complexity of pulmonary microstructures, resulting in decreased K_{app} values in the smoke-exposed rats. In addition, the small airways are defined as those less than 2 mm in diameter and a major site of pathology in many lung diseases (49). It contained a portion of the conducting airways as well as all the acinar airways. The prolonged smoke was associated with progressive pathological changes in the airway disease, such as luminal occlusion by mucus, smooth muscle hypertrophy, reduction in luminal diameter from inflammatory infiltrates, or airway wall thickening (50,51), which could increase the complexity of the pulmonary parenchyma. It would reduce the difference of K_{app} values between the smoke-exposed rats and the healthy rats. It may be was the reason that the difference of D_{app} ($P = 0.027$) between the smoke-exposed rats and the healthy rats was more significant than that of K_{app} ($P = 0.039$). Therefore, the K_{app} was also possibly related to the structure of small airways.

The traditional D_{app} was relevant to the HP gas (^{3}He or ^{129}Xe) used in the experiment. Due to the heavier atomic weight, the self-diffusion coefficient of pure xenon gas

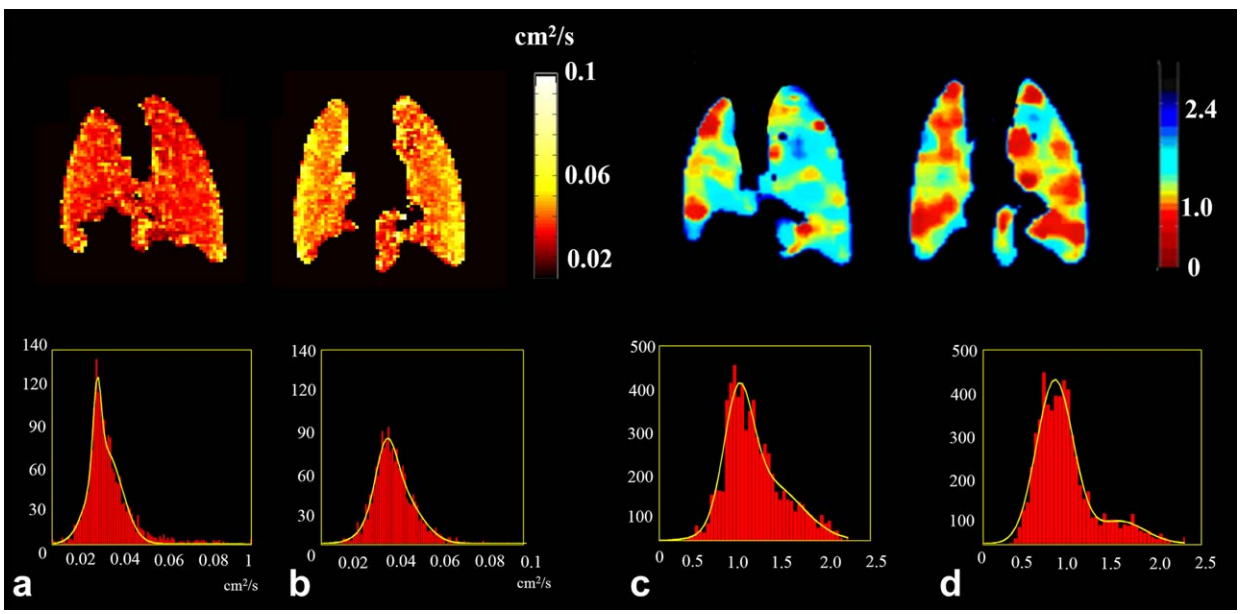

FIG. 6. Representative pulmonary parenchymal D_{app} maps (**a, b**) and K_{app} maps (**c, d**) from a smoke exposed rat (b, d) and a healthy rat (a, c). The corresponding histograms are also shown under the maps.

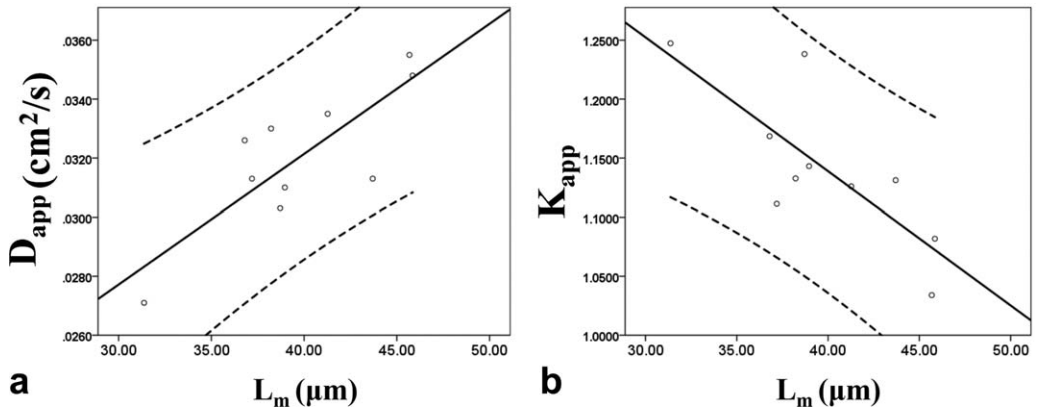

FIG. 7. Linear correlation fittings with D_{app} versus the L_m from histology (**a**) and K_{app} versus the L_m from histology (**b**). Solid lines represent linear regression lines, and dashed lines represent 95% confidence intervals for the fit.

($0.06\,cm^2/s$) was nearly 30 times less than that of pure helium gas ($1.80\,cm^2/s$) (21). Therefore, there was no comparability of the D_{app} values obtained by the two different HP gases. In contrast, the K_{app} was regarded as a measurement of the variability and intricacy of the tissue structure (48), and it probably had little relation to the magnitude of the intrinsic HP gas diffusivity. Therefore, due to the more limited pulmonary airspace in rats than in humans, the K_{app} values in the control rats in our study with HP xenon (1.1823 ± 0.0603) were much larger than those in the healthy subjects (0.3430 ± 0.0290) in a previous study of helium pulmonary DKI (7). The comparison of K_{app} would be possible even though different HP gas were used.

Valid Application of DKI

Jacob et al. (24) theoretically analyzed the conditions for the valid application of the DKI approach and found that they could be defined in terms of a critical b value b_c, or an approximate limit beyond which the DKI approach would be not correct. In the second part of our experiment, in order to study b_c, the maximum b value was increased to 80 s/cm^2, and the corresponding gradient strength was nearly 375 mT/m. The fitting results demonstrated that the DKI was still applicable to describe the non-Gaussian diffusion of HP xenon in the lungs of rats ($R^2 > 0.97$). In fact, due to the limitation of the gradient strength in clinical studies, the maximum b value applied in human studies is very limited according to Equation 2. Assuming a diffusion time of 5 ms and a constant time of 5 ms for the gradient pulse, while ignoring the gradient ramp time, the maximum b value is only 72 s/cm^2 with a maximum gradient strength of 40 mT/m, which can be achieved with a state-of-the-art human MRI scanner (21). In this manner, the DKI model would be completely valid.

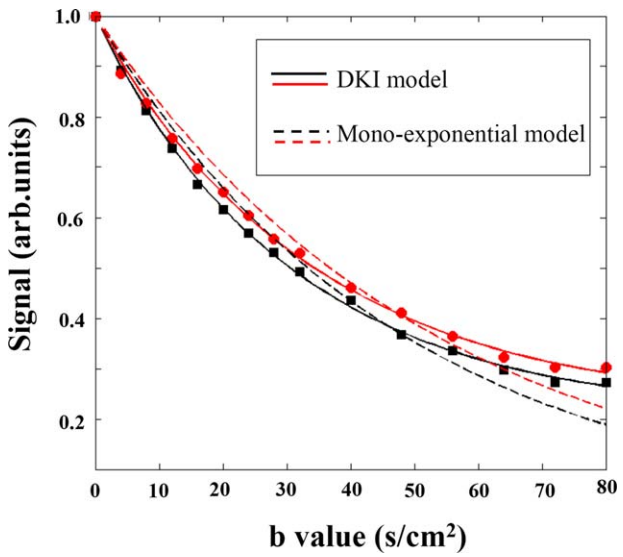

FIG. 8. Signal intensities versus b values were plotted in the second part of the experiment. The signal intensities were normalized from the pulmonary parenchyma in the two healthy rats. The solid lines were obtained by DKI model fit, while the dotted lines were obtained by the monoexponential model. Note the excellent fitting degree of the solid lines. The R^2 values were 0.9718 (red solid line) and 0.9774 (black solid line).

Limits and Outlook

There are some limits in the current experiment. To improve the image SNR, nonslice selection was used here. The rats were lying down on the scanning bed during the experiment. The gravitational effect of xenon gas and the heterogeneity of the structure existed in the coronal direction, which probably affect the signal deviation from monoexponential behavior and the measurement of K_{app} values. In future studies, the 3D or multislice 2D experiments will be attempted in DKI measurements to reduce these effects. Additionally, the histological sections were acquired from the 2D flat structure of the pulmonary parenchyma. The 2D plan images could not distinguish the alveoli and small airways accurately. Therefore, it is difficult to directly analyze the precise relationship between the DKI and the specific microstructural features (i.e., airways versus alveoli) observed in the histological sections. In future studies, a high-resolution animal CT could be used to obtain the 3D images of the global lungs, which would be useful for the accurately analysis of the results.

Yablonskiy and colleagues established quantitative relationships between lung morphology and HP gas diffusion MRI according to a simplified lung model (i.e., alveolar-covered acinar airways model). The morphological

parameters, such as the R (outer airway length), r (inter airway length), and h (depth of the alveolar) can be extracted in vivo with hyperpolarized gas multi-b diffusion MRI (20,21,52,53). However, the K_{app} was not related to specific physiological parameters, although the DKI model could well describe the non-Gaussian diffusion of HP xenon in the lungs. Future studies will focus on the precisely quantitative relationship between the DKI and the microstructure. Compared with ^{3}He, ^{129}Xe has a lower gyromagnetic ratio ($\gamma = -11.7$ MHz/T for ^{129}Xe, $\gamma = -32.4$ MHz/T for ^{3}He) and a slower diffusion rate (9,21). Moreover, it is more difficult to be polarized. All of these factors lead to a lower image SNR on the HP xenon diffusion MRI, and it is very difficult to obtain thin slice pulmonary images. Thus, it is necessary to obtain higher xenon spin polarization. In future experiments, closely coupled multichannel receive arrays (54) and parallel imaging techniques could also be adopted, and the newly presented HP gas MRI methods could also be combined (47,55,56) to acquire high image SNR and resolution. It will be possible for HP xenon DKI to detect the local changes in the pulmonary microstructure accurately and noninvasively.

CONCLUSION

In conclusion, the HP xenon diffusion in the lungs has shown a non-Gaussian characteristic due to the complex pulmonary microstructure, and the traditional ADC calculation by a single b value was no longer accurate to describe the diffusion, especially for large b values. In this study, it was demonstrated for the first time that the DKI model could describe the non-Gaussian diffusion of HP xenon in the lungs of rats very well ($R^2 > 0.9$). Moreover, the D_{app} and K_{app} parameters extracted by DKI showed significant changes in the five smoke-exposed rats compared with those in the control group, and histology revealed strong correlations with the L_m. It suggested that the DKI with hyperpolarized xenon was proper and sensitive to detect the pulmonary lesions induced by smoke, including the diseases of moderate emphysema and small airways. The measurement of K_{app} values was probably independent of the HP gas (^{3}He or ^{129}Xe) used in the experiment and highly related to the tissue microstructure, mainly the complexity or restriction. In the second part of the experiment, the DKI model still fitted the nonexponential signal decay very well ($R^2 > 0.97$), although the maximum b value was increased to 80 s/cm^2. It manifested that the critical b values would be hardly exceeded due to the limited gradient strength of the present MRI scanner. Future studies will focus on exploring the precisely quantitative relationships between DKI and the pulmonary morphology, as well as the detection and accurate location of early pulmonary changes induced by smoke with hyperpolarized xenon DKI MRI.

REFERENCES

1. Viegi G, Scognamiglio A, Baldacci S, Pistelli F, Carrozzi L. Epidemiology of chronic obstructive pulmonary disease (COPD). Respiration 2001;68:4-19.
2. Hecht SS. Tobacco carcinogens, their biomarkers and tobacco-induced cancer. Nat Rev Cancer 2003;3:733-744.
3. Ambrose JA, Barua RS. The pathophysiology of cigarette C-V smoking and cardiovascular disease—An update. J Am Coll Cardiol 2004;43:1731-1737.
4. Marsh S, Aldington S, Shirtcliffe P, Weatherall M, Beasley R. Smoking and COPD: what really are the risks? Eur Respir J 2006;28:883-884.
5. Rabe KF, Hurd S, Anzueto A, et al. Global strategy for the diagnosis, management, and prevention of chronic obstructive pulmonary disease—GOLD executive summary. Am J Respir Crit Care Med 2007;176:532-555.
6. de la Hoz RE, Berger KI, Klugh TT, Friedman-Jimenez G, Goldring RM. Frequency dependence of compliance in the evaluation of patients with unexplained respiratory symptoms. Respir Med 2000;94:221-227.
7. Trampel R, Jensen JH, Lee RF, Kamenetskiy I, McGuinness G, Johnson G. Diffusional kurtosis imaging in the lung using hyperpolarized ^{3}He. Magn Reson Med 2006;56:733-737.
8. Newell JD, Hogg JC, Snider GL. Report of a workshop: quantitative computed tomography scanning in longitudinal studies of emphysema. Eur Respir J 2004;23:769–775.
9. Moller HE, Chen XJ, Saam B, Hagspiel KD, Johnson GA, Altes TA, de Lange EE, Kauczor HU. MRI of the lungs using hyperpolarized noble gases. Magn Reson Med 2002;47:1029-1051.
10. Zhou X. Hyperpolarized noble gases as contrast agents. In: Schröder L, Faber C, editors. In vivo NMR imaging. New York, NY: Humana Press; 2011. p 189-204.
11. Mugler JP, Altes TA. Hyperpolarized 129Xe MRI of the human lung. J Magn Reson Imaging 2013;37:313–331.
12. Korchak SE, Kilian W, Mitschang L. Configuration and performance of a mobile 129Xe polarizer. Appl Magn Reson 2013;44:65-80.
13. Kruger SJ, Niles DJ, Dardzinski B, et al. Hyperpolarized helium-3 MRI of exercise-induced bronchoconstriction during challenge and therapy. J Magn Reson Imaging 2014;39:1230-1237.
14. de Lange EE, Mugler JP, Brookeman JR, Knight-Scott J, Truwit JD, Teates CD, Daniel TM, Bogorad PL, Cates GD. Lung air spaces: MR imaging evaluation with hyperpolarized ^{3}He gas. Radiology 1999;210:851-857.
15. Sukstanskii AL, Quirk JD, Yablonskiy DA. Probing lung microstructure with hyperpolarized ^{3}He gradient echo MRI. NMR Biomed 2014;27:1451-1460.
16. Chen XJ, Hedlund LW, Moller HE, Chawla MS, Maronpot RR, Johnson GA. Detection of emphysema in rat lungs by using magnetic resonance measurements of ^{3}He diffusion. Proc Natl Acad Sci U S A 2000;97:11478-11481.
17. Mata JF, Altes TA, Cai J, et al. Evaluation of emphysema severity and progression in a rabbit model: comparison of hyperpolarized ^{3}He and ^{129}Xe diffusion MRI with lung morphometry. J Appl Physiol 2007;102:1273-1280.
18. Altes TA, Mata J, de Lange EE, Brookeman JR, Mugler JP. Assessment of lung development using hyperpolarized helium-3 diffusion MR imaging. J Magn Reson Imaging 2006;24:1277-1283.
19. Kaushik SS, Cleveland ZI, Cofer GP, et al. Diffusion-weighted hyperpolarized ^{129}Xe MRI in healthy volunteers and subjects with chronic obstructive pulmonary disease. Magn Reson Med 2011;65:1154-1165.
20. Yablonskiy DA, Sukstanskii AL, Leawoods JC, Gierada DS, Bretthorst GL, Lefrak SS, Cooper JD, Conradi MS. Quantitative in vivo assessment of lung microstructure at the alveolar level with hyperpolarized ^{3}He diffusion MRI. Proc Natl Acad Sci U S A 2002;99:3111-3116.
21. Yablonskiy DA, Sukstanskii AL, Quirk JD, Woods JC, Conradi MS. Probing lung microstructure with hyperpolarized noble gas diffusion MRI: theoretical models and experimental results. Magn Reson Med 2014;71:486-505.
22. Wang W, Nguyen NM, Yablonskiy DA, Sukstanskii AL, Osmanagic E, Atkinson JJ, Conradi MS, Woods JC. Imaging lung microstructure in mice with hyperpolarized He-3 diffusion MRI. Magn Reson Med 2011;65:620-626.
23. Parameswaran H, Bartolak-Suki E, Hamakawa H, Majumdar A, Allen PG, Suki B. Three-dimensional measurement of alveolar airspace volumes in normal and emphysematous lungs using micro-CT. J Appl Physiol 2009;107:583-592.
24. Jacob RE, Laicher G, Minard KR. 3D MRI of non-Gaussian 3He gas diffusion in the rat lung. J Magn Reson 2007;188:357-366.
25. Phillips J, Charles-Edwards GD. A simple and robust test object for the assessment of isotropic diffusion kurtosis. Magn Reson Med 2015;73:1844–1851.
26. Tanner JE, Stejskal EO. Restricted self-diffusion of protons in colloidal systems by pulsed-gradient spin-echo method. J Chem Phys 1968;49:1768-1777.

27. Jensen JH, Helpern JA, Ramani A, Lu HZ, Kaczynski K. Diffusional kurtosis imaging: the quantification of non-Gaussian water diffusion by means of magnetic resonance imaging. Magn Reson Med 2005;53: 1432-1440.
28. Falangola MF, Jensen JH, Babb JS, Hu C, Castellanos FX, Di Martino A, Ferris SH, Helpern JA. Age-related non-Gaussian diffusion patterns in the prefrontal brain. J Magn Reson Imaging 2008;28:1345-1350.
29. Jansen JFA, Stambuk HE, Koutcher JA, Shukla-Dave A. Non-Gaussian analysis of diffusion-weighted MR imaging in head and neck squamous cell carcinoma: a feasibility study. AJNR Am J Neuroradiol 2010;31:741-748.
30. Suo S, Chen X, Ji X, Zhuang Z, Wu L, Yao Q, Fan Y, Xu J. Investigation of the non-Gaussian water diffusion properties in bladder cancer using diffusion kurtosis imaging: a preliminary study. J Comput Assist Tomogr 2015;39:281-285.
31. Huang Y, Chen X, Zhang Z, Yan L, Pan D, Liang C, Liu Z. MRI quantification of non-Gaussian water diffusion in normal human kidney: a diffusional kurtosis imaging study. NMR Biomed 2015;28:154-161.
32. Tamura C, Shinmoto H, Soga S, Okamura T, Sato H, Okuaki T, Pang YX, Kosuda S, Kaji T. Diffusion kurtosis imaging study of prostate cancer: preliminary findings. J Magn Reson Imaging 2014;40:723-729.
33. Zhou X, Luo J, Sun X, Zeng X, Zhan M, Ding S, Liu M. Experiment and dynamic simulations of radiation damping of laser-polarized liquid ^{129}Xe at low magnetic field in a flow system. Appl Magn Reson 2004;26:327-337.
34. Zeng X, Wu C, Zhao M, Li S, Li L, Zhang X, Liu Z, Liu W. Laser-enhanced low-pressure gas NMR signal from ^{129}Xe. Chem Phys Lett 1991;182:538-540.
35. Zhou X, Mazzanti ML, Chen JJ, Tzeng YS, Mansour JK, Gereige JD, Venkatesh AK, Sun Y, Mulkern RV, Albert MS. Reinvestigating hyperpolarized ^{129}Xe longitudinal relaxation time in the rat brain with noise considerations. NMR Biomed 2008;21:217-225.
36. Driehuys B, Cates GD, Miron E, Sauer K, Walter DK, Happer W. High-volume production of laser-polarized Xe-129. Appl Phys Lett 1996;69:1668-1670.
37. Bai J, Qiu SL, Zhong XN, Huang QP, He ZY, Zhang JQ, Liu GN, Li MH, Deng JM. Erythromycin enhances CD4+Foxp3+regulatory T-cell responses in a rat model of smoke-induced lung inflammation. Mediators Inflamm 2012;2012:410232.
38. Baum JA. The carrier gas in anaesthesia: nitrous oxide/oxygen, medical air/oxygen and pure oxygen. Curr Opin Anaesthesiol 2005;17:513-516.
39. Xin Y, Enami K, Kadlecek SJ, Mongkolwisetwara P, Kuzma NN, Profka H, Xu Y, Hamedani H, Pullinger BM, Ghosh RK, et al. Imaging of Lung Micromechanics with Hyperpolarized Gas Diffusion MRI: Regional Compliace. In Proceedings of the 19th Annual Meeting of ISMRM, Montreal, Canada, 2011. p. 549.
40. Boudreau M, Xu X, Santyr GE. Measurement of ^{129}Xe gas apparent diffusion coefficient anisotropy in an elastase-instilled rat model of emphysema. Magn Reson Med 2013;69:211-220.
41. Li H, Zhang Z, Zhao X, Sun X, Ye C, Zhou X. Quantitative evaluation of radiation-induced lung injury with hyperpolarized xenon magnetic resonance. Magn Reson Med 2016;76:408-416.
42. Ouriadov A, Farag A, Kirby M, McCormack DG, Parraga G, Santyr GE. Lung morphometry using hyperpolarized 129Xe apparent diffusion coefficient anisotropy in chronic obstructive pulmonary disease. Magn Reson Med 2013;70:1699-1706.
43. Ruan W, Zhong J, Wang K, Wu G, Han Y, Sun X, Ye C, Zhou X. Detection of the mild emphysema by quantification of lung respiratory airways with hyperpolarized xenon diffusion MRI. J Magn Reson Imaging. doi: 10.1002/jmri.25408.
44. Otsu N. Threshold selection method from gray-level histograms. IEEE Trans Syst Man Cybern 1979;9:62-66.
45. Qu WS, Yin JY, Wang HM, Dong YS, Ding RG. A simple method for the formalin fixation of lungs in toxicological pathology studies. Exp Toxicol Pathol 2015;67:533-538.
46. Woods JC, Choong CK, Yablonskiy DA, Bentley J, Wong J, Pierce JA, Cooper JD, Macklem PT, Conradi MS, Hogg JC. Hyperpolarized ^{3}He diffusion MRI and histology in pulmonary emphysema. Magn Reson Med 2006;56:1293-1300.
47. Deng H, Zhong J, Ruan W, Chen X, Sun X, Ye C, Liu M, Zhou X. Constant-variable flip angles for hyperpolarized media MRI. J Magn Reson 2016;263:92-100.
48. Palombo M, Gentili S, Bozzali M, Macaluso E, Capuani S. New insight into the contrast in diffusional kurtosis images: does it depend on magnetic susceptibility? Magn Reson Med 2015;73:2015-2024.
49. McNulty W, Usmani OS. Techniques of assessing small airways dysfunction. Eur Clin Respir J. 2014;1:10.3402/ecrj.v1.25898.
50. Cosio MG, Hale KA, Niewoehner DE. Morphological and morphometric effects of prolonged cigarette smoking on small airways. Am Rev Respir Dis 1980;122:265-271.
51. Dogan OT, Elagoz S, Ozsahin SL, Epozturk K, Tuncer E, Akkurt I. Pulmonary toxicity of chronic exposure to tobacco and biomass smoke in rats. Clinics 2011;66:1081-1087.
52. Sukstanskii AL, Yablonskiy DA. Lung morphometry with hyperpolarized ^{129}Xe: theoretical background. Magn Reson Med 2012;67:856-866.
53. Lee RF, Johnson G, Stefanescu C, Trampel R, McGuinness G, Stoeckel B. A 24-ch phased-array system for hyperpolarized helium gas parallel MRI to evaluate lung functions. In Proceedings of the IEEE-EMBS 27th Annual International Conference, Shanghai, China, 2005. p. 4278.
54. Ouriadov A, Fox M, Hegarty E, Parraga G, Wong E, Santyr GE. Early stage radiation-induced lung injury detected using hyperpolarized ^{129}Xe morphometry: proof-of-concept demonstration in a rat model. Magn Reson Med 2016;75:2421–2431.
55. Collier GJ, Wild JM. In vivo measurement of gas flow in human airways with hyperpolarized gas MRI and compressed sensing. Magn Reson Med 2015;73:2255-2261.
56. Zhong J, Ruan W, Han Y, Sun X, Ye C, Zhou X. Fast determination of flip angle and T_1 in hyperpolarized gas MRI during a single breath-hold. Sci Rep 2016;6:25854.